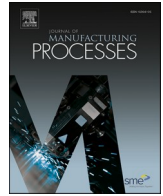




Contents lists available at ScienceDirect

## Journal of Manufacturing Processes

journal homepage: [www.elsevier.com/locate/manpro](http://www.elsevier.com/locate/manpro)

## 3D metal freeform micromanufacturing

Luciano Borasi<sup>a,\*</sup>, Enrico Casamenti<sup>b,\*</sup>, Raphaël Charvet<sup>a</sup>, Cyril Dénéreaz<sup>a</sup>,  
Sacha Pollonghini<sup>b</sup>, Léa Deillon<sup>a</sup>, Tao Yang<sup>b</sup>, Fatmah Ebrahim<sup>b</sup>, Andreas Mortensen<sup>a</sup>,  
Yves Bellouard<sup>b</sup>

<sup>a</sup> Laboratory of Mechanical Metallurgy (LMM), STI, IMX, École Polytechnique Fédérale de Lausanne (EPFL), CH-1015 Lausanne, Switzerland

<sup>b</sup> Galatea Laboratory, STI, IEM, École Polytechnique Fédérale de Lausanne (EPFL), CH-2002 Neuchâtel, Switzerland

## ARTICLE INFO

## Keywords:

Micro-manufacturing  
Freeform fabrication  
Microcasting  
Femtosecond laser

## ABSTRACT

Despite remarkable progress made in recent years, producing freeform three-dimensional micro-components out of copper, silver or gold and their alloys remains an engineering challenge: current processes are either too slow to be economically viable, or produce porous or otherwise imperfect metal microstructures. Here we introduce an alternative, faster approach for the freeform fabrication of metal micro-components amenable to the processing of noble metals. The process begins with the 3D, micron-resolution, carving of arbitrarily shaped interconnected molds into amorphous silica using femtosecond laser micromachining and selective etching. This is followed by pressure infiltration of the mold with the molten metal, which is subsequently solidified. Metal architectures produced by this process have micron-scale resolution, are fully freeform and multiscale in geometry, and are made of dense metal, while the process speed largely exceeds what is achieved in current alternative metal microfabrication approaches. The resulting glass/metal combinations enable new micro-device architectures. Alternatively, by mold dissolution, self-standing micron-scale 3D metal parts are produced, of high metallurgical quality and with features sizes down to  $\sim 2 \mu\text{m}$ .

## 1. Introduction

Many domains of technological progress, including micro-electromechanical systems (MEMS), microsensors, metamaterials, integrated optical devices, microfluidic, medtech micro-components, or microelectronic devices, rely on the availability of geometrically complex structures made to micrometric resolution [1]. Most established manufacturing processes at such a small scale have geometrical constraints that limit them to two dimensions or to particular geometry types with specific symmetry properties, such as cylindrical or spherical. The production of truly freeform 3D shapes at the microscale, i.e. with no geometrical constraint across all three spatial dimensions, with micron to sub-micron resolution, has been an ongoing quest for decades, starting with pioneering work in advanced 3D-lithography on polymers [2–4]. Alternative routes for three-dimensional freeform micro-manufacturing, based on negative processes where the material is selectively removed, have been successfully applied to glass [5–7]. Some of these processes are now commercially available.

Comparatively, the 3D freeform production of metallic structures to

a micron and sub-micron level of precision remains challenging. Current selective powder-melting or sintering methods do not reach such resolutions, smallest features achievable being currently limited by the size of the powder to roughly  $20 \mu\text{m}$  [8]. Other methods fit for the production of metallic micro-components include the electroplating-based LIGA process [9,10], micro-beam machining [11–13], micro/nano-forming [14] and processes that add metal to the surface of patterned glass [15–18]. None of these technologies, however, provides full geometrical design freedom in all three dimensions. To these, recent years have seen the addition of a wide range of novel, generally still experimental but truly three-dimensionally freeform, additive manufacturing processes, of which a detailed and extensive recent review can be found in References [19,20].

Current cutting-edge additive 3D freeform micromanufacturing processes include (i) metal-ink 3D printing followed by annealing, metal lift and deposition, (ii) locally triggered chemical vapor deposition or chemical reaction, as well as (iii) high-precision in-situ electrolytic deposition. Most of these 3D metal additive micromanufacturing methods afford full 3D design freedom, but often produce parts of

\* Corresponding authors.

E-mail addresses: [luciano.borasi@epfl.ch](mailto:luciano.borasi@epfl.ch) (L. Borasi), [enrico.casamenti@epfl.ch](mailto:enrico.casamenti@epfl.ch) (E. Casamenti).

<sup>1</sup> These authors contributed equally to this work.

<https://doi.org/10.1016/j.jmapro.2021.06.002>

Received 23 March 2021; Received in revised form 1 June 2021; Accepted 1 June 2021

1526-6125/© 2021 The Author(s). Published by Elsevier Ltd on behalf of The Society of Manufacturing Engineers. This is an open access article under the CC BY

license (<http://creativecommons.org/licenses/by/4.0/>).

porous or irregularly shaped metal (e.g., [21–26]), with the exception of local electrodeposition methods, which have in recent years demonstrated the production of complex, high aspect ratio, smooth-surface 3D freeform structures of dense metal shaped to sub-micrometric resolution [19,20,27–29]. Point-by-point local electroplating has, however, the limitation that volumetric metal deposition rates remain low, limiting that method to prototyping or niche applications.

We present here an alternative approach that enables the fabrication of dense noble metal micro-components to micrometric resolution and has the potential for far higher production rates than current alternative processes: multiscale structures of size up to a few millimeters that have micron-scale features, unprecedented 3D complexity and sub-micron surface roughness are demonstrated. In this approach, freeform processing is first conducted in subtractive mode, starting with a glass substrate that is carved, using 3D femtosecond (fs) laser micro-fabrication followed by selective etching, to create a hollow that has the shape of the metal structure that one aims to produce. The hollow is then filled with molten silver, copper, gold or their alloys. This is achieved using elevated-temperature pressure infiltration to create, once the metal has solidified, what amounts to a cast metal structure freely shaped to micrometric resolution.

Seen differently, the present process is indeed a miniaturized variant of metal casting. Metal casting has resisted miniaturization down to sub-millimeter size scales mainly because, at the microscale and at the elevated temperatures characteristic of molten engineering metals (on the order of 1000 °C), capillarity coupled with high atom mobility rates interfere to disrupt the process. Interference of these phenomena with the casting process is manifest on three fronts:

- (i) Capillary forces oppose metal ingress into fine-scale mold cavities because molten metals have high surface tensions and wet poorly nearly all ceramics [30];
- (ii) Capillary forces coupled with high atom mobility at metal casting temperatures deform the surface of crystalline mold materials conventionally used to make precision molds. Indeed, wherever the mold surface intersects crystal defects (dislocations, interfaces or grain boundaries), capillary force equilibration creates micron-scale depressions along the mold surface. Those depressions matter little in conventional macroscale casting; at the microscale, however, once filled with metal, such depressions become as many unwanted, comparatively large, protuberances along the cast metal surface.
- (iii) At temperatures such as 1000 °C, chemical reaction rates are high. This leads to an additional limitation, namely that there must be no chemical affinity between atoms that make the mold and those that make the metal.

We overcome here the first physical limitation (i) by pressurizing the hot molten metal in a way that forces it against capillary forces to fill micron-scale mold cavities. We address the second limitation (ii) by using an amorphous, and hence microstructurally featureless, material, namely glass, to make the mold. Finally, we overcome the chemical limitation (iii) by working with metals made of elements that have an oxide less stable than that of silicon; this includes noble metals, which are of prime interest in microtechnology by virtue of their corrosion resistance and high conductivity.

With those features, the present process goes well beyond previous attempts to push down the resolution of metal casting. Those have produced parts on the order of a few tenths of millimeter ( $\sim 100 \mu\text{m}$ ) in size, but have not reached micrometric freeform resolution [31–34], or are restricted to casting one of the few metals or alloys that melt near room temperature [35].

## 2. Results

Process steps that lead to produce 3D structures of dense engineering

noble metal with sub-micron resolution are detailed in Fig. 1. As an illustration, we show the production of a micrometric classroom containing a series of miniature chairs and desks. Step 1 in Fig. 1 consists in exposing quartz glass to femtosecond laser irradiation according to a freely designed interconnected geometrical pattern that defines the material to be removed by altering locally the glass structure. This alteration causes the glass to be preferentially etched where it has been exposed to laser irradiation.

This process is based on nonlinear absorption phenomena. These events are observed in otherwise transparent substrates when the incoming laser beam *locally* exceeds a peak irradiance level (typically around  $\text{GW}/\text{mm}^2$ ), triggering a chain of events leading to the ionization of the matter. As the effect is non-linear and depends on a threshold value, the effective size of the ionized volume can be smaller than the beam waist itself and the laser wavelength [5–7]. In addition, given the extremely short plasma life time, the absorbed energy remains confined in the focal volume and no heat is transfer to the surrounding, which thus remain largely unaffected [36,37]. Combined with high-accuracy beam trajectory thanks to the use of high precision motorized stages (PI Micos with a repeatability of 200 nm over a centimeter motion range and a micron over the full travel range), it enables the engraving of arbitrary 3D-shapes made of single voxel sizes that depends chiefly on the confocal parameters and the pulse energy. In our case, considering a beam waist at focus of 1.9  $\mu\text{m}$  and a moderately focused beam with an energy of about 240 nJ, a voxel of laser-modified volume has an ellipsoid shape with 1.9  $\mu\text{m}$  and 8  $\mu\text{m}$  on the short and long axis, respectively. Smaller voxel sizes can be achieved by lowering further the pulse energy.

In Fig. 1 step 2 wet chemical etching of the substrate preferentially removes those regions that were modified by the laser along a path that intersects the mold free surface. The etching-rate contrast between pristine and modified mold material depends on the chemistry used (namely, with fused quartz, etching with a basic – KOH [38] – or with an acidic – HF [6,7] – solution), on the deposited energy (or net fluence), and on other laser-related parameters such as the laser-beam polarization or the pulse duration [39]. By precisely controlling the exposure and the etching steps, it is thus possible to achieve micrometric resolutions in the mold manufacturing. As the etching front progresses inward from the mold surface through the exposed pattern, the final shape of the etched volume becomes diffusion-limited and shows a dependence on the etching rate contrast between pristine and exposed material. This may lead to a dependence of the etched geometry on the time of exposure to the chemical solution, to be compensated for in the design of the path followed by the fs-laser beam.

Filling of the cavities with the metal, Steps 3 to 5 (Fig. 1), is performed by applying external pressure on the liquid metal sufficient to overcome capillary forces at play and make it flow into the mold. This is achieved using pressurized gas. In experiments reported here, the metal to be infiltrated is placed on top of the substrate, over all exposed cavities. The chamber is evacuated, then kept under a low vacuum and heated up to slightly above the melting point ( $T_m$ ) of the metal to be cast. Once it is molten, the metal covers and seals all mold entries along the upper mold surface. At this point, a non-reactive gas, typically argon, is bled into the chamber. As the gas pressure builds up, the pressure it exerts on the metal eventually drives the latter to flow into the (evacuated) cavities of the mold, filling them. Once the mold is full, mold and metal are cooled to solidify the metal. In doing this, particular consideration must be given to feed metal solidification shrinkage, a classical challenge in casting also present at the microscale. To this end, directional metal cooling is used; this is done by placing a chill in contact with the apparatus along the substrate side opposite to the metal drop. One must also avoid the formation of cracks that may appear in the brittle glass substrate under the action of thermal stresses associated with the difference in coefficients of thermal expansion (CTE) between metal (typically  $\sim 10\text{--}20 \mu\text{m m}^{-1} \text{K}^{-1}$ ) and substrate ( $\sim 0.5 \mu\text{m m}^{-1} \text{K}^{-1}$ ). Such cracks were observed in some of our experiments through standard and

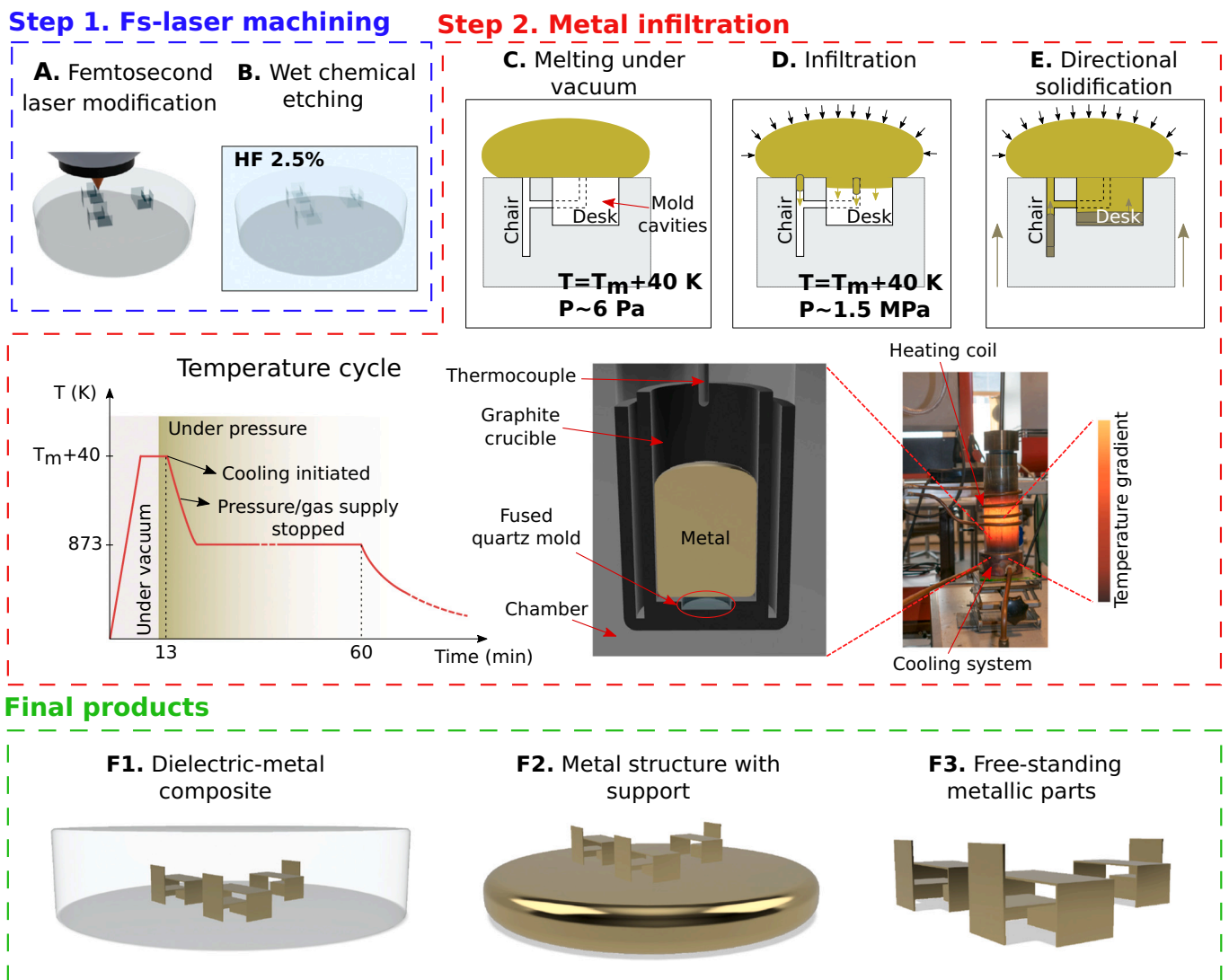


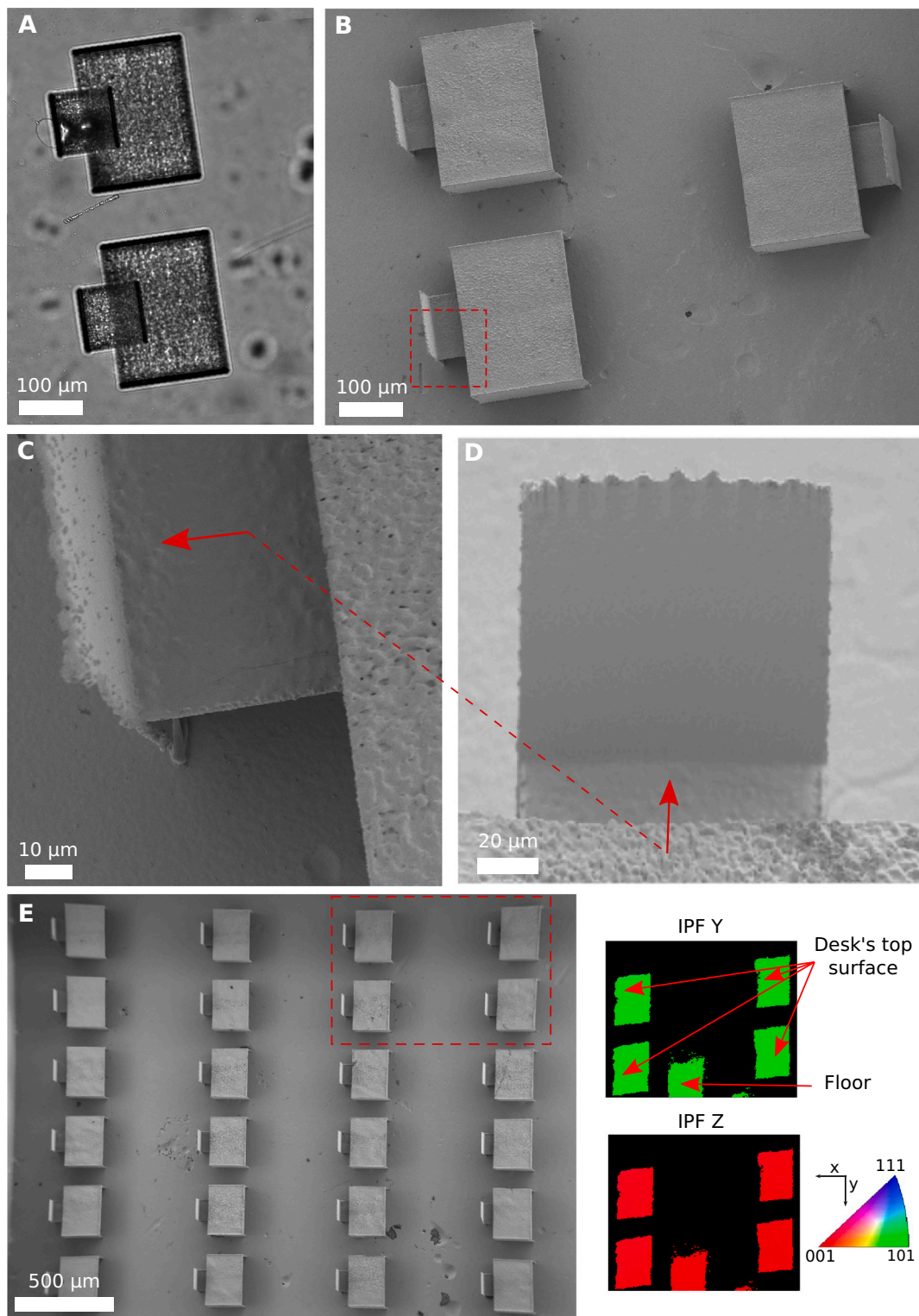
**Fig. 1.** Schematic of the microcasting process. The process comprises two main sequences, one being fs-laser 3D micromachining, and the second being metal pressure infiltration. Step 1 – a pattern defining the 3D structure is inscribed within a fused quartz substrate using a fs-laser. Step 2 - the substrate undergoes wet chemical etching to dissolve interconnected laser-patterned regions that intersect the substrate surface, thus turning the fused quartz substrate into a mold to be filled with metal. Step 3 - the fused quartz mold is positioned in the infiltration chamber, together with a metal load placed over the exposed cavities; the chamber is evacuated and the temperature is raised to melt the metal. Step 4 - pressurized inert gas pushes the metal against capillary forces, driving it to fill the pre-evacuated hollows. Step 5 - while maintaining the pressure, the chamber is put in contact with a chill to promote directional solidification. Step 6 - different final microscopic products can be obtained by varying final steps in the process.

cross-polarized optical microscopy; they are avoided by means of slow cooling after infiltration.

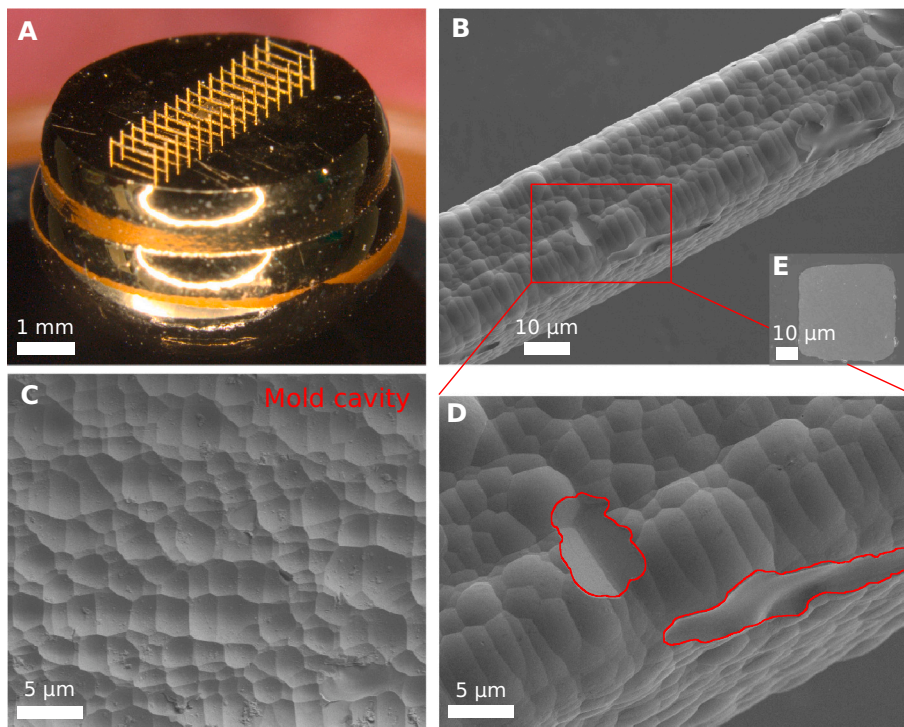
After solidification (Fig. 1 Step 6), a substrate-metal composite is produced. The excess metal can be removed to obtain a microscopic fused quartz/metal composite structure that can, in itself, be of interest in microengineering device fabrication (Fig. 1 Step 6A). Alternatively, to produce a loose metal casting, the glass mold is dissolved in an etchant to which the metal is inert (for example, an aqueous HF solution when casting silver). Demolding -in the terminology of casting- can either produce miniature structures that are linked to a bulk metal base (Fig. 1 Step 6B), or if Steps 6A and 6B are combined, it will yield many separated miniature metal castings (Fig. 1 Step 6C).

Fig. 2 displays images of such a tiny classroom composed of desks and chairs, all made of pure silver. This particular assembly demonstrates the ability of the present process to produce, at the microscale, complex 3D structures with a shape that is not amenable to metal micromachining. The cast structures have a thickness near  $2 \mu\text{m}$ . The similarity of chair/table pairs shows the reproducibility of the

technique, and its resolution is shown by the submicron surface roughness of the mold or casting. In this illustration, to allow for observation in the scanning electron microscope, the fused quartz substrate was dissolved after solidification; this left the final metal chair and table structures linked to the silver that remained above the substrate (as in Fig. 1 - Step 6B). Fig. 2C and D show a close inspection of one of the chairs in two different perspectives, to exhibit its thickness and contours. In particular, a rough and wavy finishing of the top edge is observed. This feature is associated with the progressing etching front after laser machining during mold preparation and is later on reproduced by the metal during infiltration and solidification. Specifically, such imperfections are found if the etching is interrupted before the entire laser-affected region is removed. It is in fact not seen on the other edges of the structures of Fig. 2 (or in subsequent figures). On the other hand, the slight roughness on the lateral edges of the chair (in Fig. 2D) derives from the laser machining trajectory followed during mold preparation and can be avoided by optimizing both the laser trajectory and the deposited energy. As shown in Fig. 2E, the metal grain size far exceeds



**Fig. 2.** Images of a cast silver miniature classroom. (A) Reveals the fused quartz substrate (i.e., the mold) after etching and before metal infiltration (Step 2 in Fig. 1). In (B) the metal structure is shown after dissolution of the mold (Step 6B in Fig. 1). (C) and (D) Details at higher magnification the area delimited by the dashed rectangle in (B), the arrow indicates the orientation of (D) with respect to (C). (E) An array of  $6 \times 4$  “chairs” and “desks” and inverse pole figures (IPF) of the four “desks” contained in the red dashed rectangle, evidencing that these, as well as the “floor” (i.e. the support), are single-crystalline metal structures. (A) Optical microscopy taken through fused quartz, (B), (C), (D) and (E) scanning electron microscopy (SEM) and (E) electron backscatter diffraction (EBSD). (For interpretation of the references to colour in this figure legend, the reader is referred to the web version of this article.)



**Fig. 3.** Images of suspended beams made of gold and left connected to the bulk metal. (A) Overall view of the piece after dissolution of the fused quartz mold. (B) SEM close-up image of a single suspended beam showing features typical of a silica glass etched with hydrofluoric acid. (C) SEM images of the internal surface of an etched, uninfiltreated mold cavity. In (D) a portion of the beam in (B) is shown to highlight likely surface casting defects in red. (E) SEM image of a cross section of a similar silver structure while it was still embedded in the fused quartz mold, showing that the beams are made of pore-free, dense metal (the corresponding silver beams can be seen in Fig. S1). (For interpretation of the references to colour in this figure legend, the reader is referred to the web version of this article.)

that of casting features, such that chairs and tables are essentially all monocrystalline – this parallels what was found with cast aluminum microwires cast using molds of grown NaCl single crystal [33].

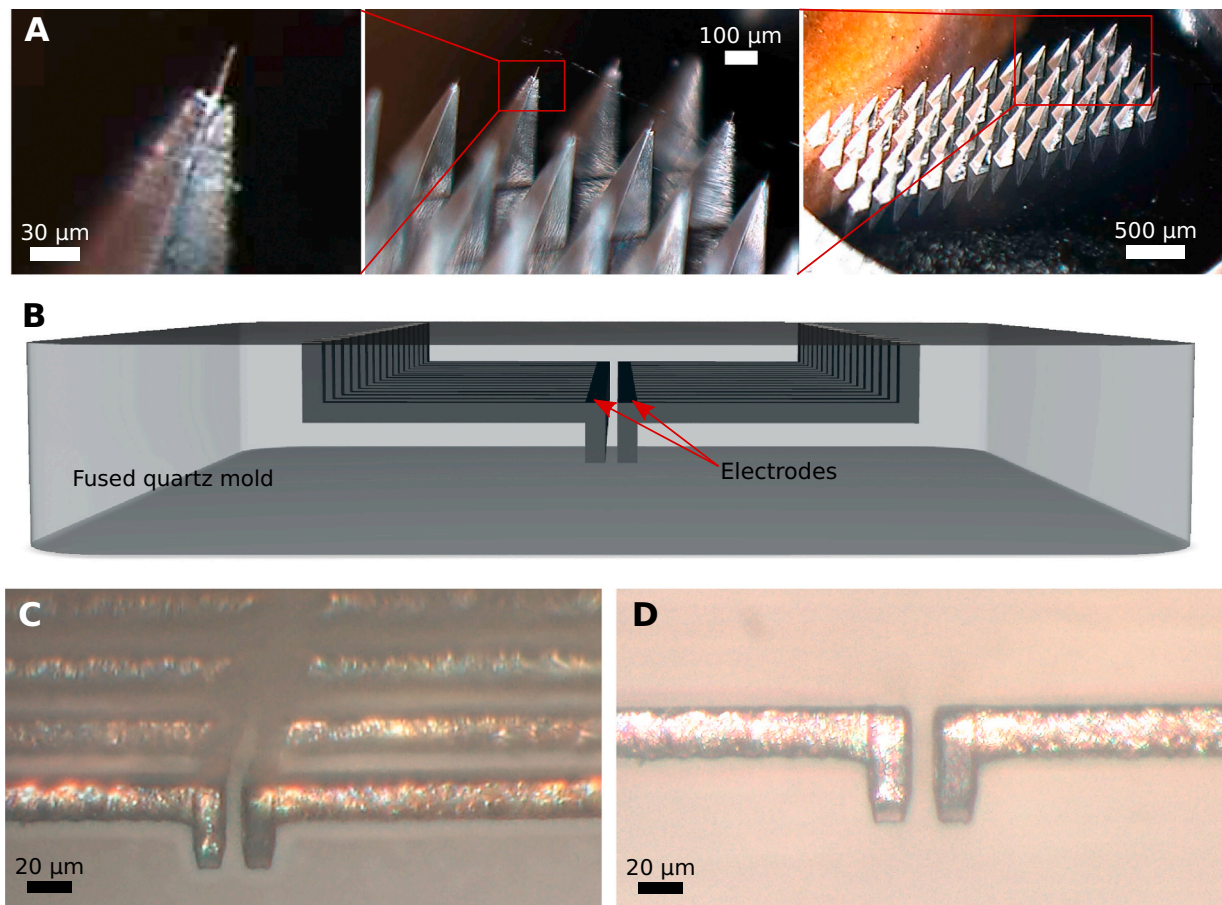
The process was also used to fabricate a set of suspended ('H-shape') beams made of pure gold, Fig. 3. The suspended beams in Fig. 3 have a  $45 \times 45 \mu\text{m}^2$  square-cross section and a length of  $900 \mu\text{m}$ , demonstrating an aspect ratio (AR) – cross-section over length - as high as 20. Furthermore, in this experiment the AR was not maximized: higher values are likely achievable. Indeed, fs-laser micromachining has demonstrated AR values that exceed 500 with only two entrance points for the etchant [40] and has no theoretical aspect ratio limit if multiple entries can be included [7]. Close inspection of the mold surface along a longitudinal cut through an un-infiltrated mold along the length of the suspended-beams (Fig. 3C) reveals features typical of fs-laser exposed silica glass etched with hydrofluoric acid: [41] note how those are later on reproduced by the gold (Fig. 3B). This demonstrates that the pressure infiltration process used here can replicate shapes with a sub- $\mu\text{m}$ -scale resolution, similar to what is obtained in polymer molding. [42] Even though the overall surfaces of the suspended beams are easily correlated to features on the mold, some peculiarities can be distinguished in some structures (red delimited areas in Fig. 3D). These depressions are particularly smooth and they interrupt surface patterns present on the fused quartz surface; hence, they may have been produced by metal solidification shrinkage or the presence of trapped gas.

Fig. 3E shows a cross section through a similar structure made of pure silver; as seen, the metal is dense, or in other words exempt of pores. To check that there is no significant chemical interaction between the mold and the metal, we investigated whether there was penetration of the metal atoms into the glass matrix using energy-dispersive X-ray spectroscopy (EDS) measurements across sections of infiltrated beams, still embedded in its fused quartz mold, near the host-substrate/metal interface. No new phase and no traces of metal within the fused quartz host were detected (see Fig. S2 in Supporting information). Local properties of the metal were measured by nanoindentation: for the pure silver of this casting, data yield a Young's modulus of  $84.1 \pm 1.2 \text{ GPa}$ , to be compared with 83 GPa for bulk silver [43], in accord with the observation that the microcast metal is fully dense. This shows that the

process produces metallurgically sound metal, the flow stress of which can be tailored by alloying. Hardness values were similarly collected, with the consideration of possible size-effects (data in Supplementary material) [44,45].

Fig. 4A exhibits an array of silver pyramids, each ending in a much thinner filament,  $30 \mu\text{m}$ -long and  $\sim 2 \mu\text{m}$  in diameter. The silver substrate was removed by mechanical grinding in order to obtain, as in Fig. 1 Step 6A, a final product consisting of the 6 mm-diameter,  $800 \mu\text{m}$ -thick, fused quartz substrate containing an array of embedded silver pyramids each topped by this thin, antenna-like, coaxial filament. This demonstrates that the combination of laser-patterning and infiltration characteristic of the process provides a pathway for the production of multiscale 3D structures that would be difficult if not impossible to achieve by other means. As another prototype giving an example of the innovation potential of the technology, Fig. 4B-D shows a 3D-array of high-aspect ratio multiscale silver-copper alloy micro-electrodes that are left embedded in the fused quartz mold (visualized here by observation through the glass). The minimum distance between electrodes is about  $6 \mu\text{m}$  and the total structure length is 5 mm (leading to an aspect ratio of the glass slit between electrodes that exceeds 800). Being able to produce such arbitrarily shaped 3D highly conductive electrodes embedded in a high dielectric constant material host is highly interesting in numerous fields of microtechnology: e.g., implantable devices in medicine, or components for high-voltage, high-frequency electronics.

Fig. 5 shows a larger, geometrically complex, 3D (Maltese cross) structure fabricated out of copper or silver. Fig. 5A-C shows the structure still embedded within fused quartz, while Fig. 5D shows the self-standing structure (here made of silver) extracted out of its mold. The beams composing the truss structure have a diameter around  $50 \mu\text{m}$ , while the entire Maltese cross fits within an area of two-by-two millimeters. In this larger casting, there was a higher probability for solidification to nucleate and propagate from different locations of the mold, leading to a polycrystalline structure. Grain boundaries are indeed revealed by the trough that capillary forces have created along the beams composing the structure (Fig. 5D). This is confirmed by EBSD, which shows the presence of three crystals in the imaged structure, grain boundaries of which are consistent with the location of grain boundary



**Fig. 4.** (A) Optical micrograph of a silver pyramid array embedded in fused quartz, each pyramid ending with a thin antenna-like filament extending from its tip, illustrating the multiscale and multi-material capability of the process. (B), (C) and (D) are images of a row of electrode pairs embedded in fused quartz. (B) CAD model of the design (for the sake of clarity, the drawing is out of scale). (C) and (D) are optical micrographs of the resulting structures of 79wt%Ag-21wt%Cu alloy embedded in fused quartz.

grooves visible in the SEM micrograph. Fig. 5C shows a larger version ( $\sim 4 \times 4$  mm) of the same design, this time infiltrated with pure copper and left embedded in fused quartz.

### 3. Discussion

Structures produced in this work, of size ranging from a few tens of micrometer to a few millimeters and with features of size down to around  $2 \mu\text{m}$ , are made out of engineering metals (silver, copper and gold and their alloys) that are among the best electrical conductors and the most corrosion resistant metals – features of interest for micro-technology in general. It will easily be appreciated that producing those structures would at best be difficult using existing technology, with one exception, namely local electrodeposition. Micromachining would not carve out the space between the tables and the chairs, or between them and the floor of the classroom of Fig. 2. Layer deposition processes would not, unless the part was of dimensions far above the voxel size, produce in-plane beams of circular cross-section such as those in Fig. 5. Processes that produce rapidly porous and/or binder-containing metal structures that require subsequent sintering and/or debinding would be unlikely to leave the thin table or chair structures unwarped after annealing. The only process that we believe could rival or surpass what is presented here is local electroplating, as this process also produces dense metal with nearly total shape flexibility (such processes might, however, be challenged by the sharp,  $90^\circ$  corner, overhangs present in structures of Figs. 2, 3 or 5).

As with any process that aims at broad acceptance and potential

industrialization, achievable production rates are important. In producing silica molds in larger quantities, the laser-exposure time is the main bottleneck.

The time needed to produce the mold for samples presented here was, with laboratory tooling used in this study, on the order of a day for a part such as the Maltese cross in Fig. 5. In our laboratory, etching represented most of this time. In a production environment, however, the etching process is low-cost and usually parallelized, such that it does not represent an intrinsic limitation on production rates. Casting, meaning pressure infiltration followed by metal solidification, is a relatively rapid process already capable of high production rates; it, too, can also be massively parallelized, since larger molds each containing many castings can be infiltrated, solidified and retrieved simultaneously. Femtosecond laser-exposure is therefore the rate-limiting step of the present process if production runs reach sufficiently high volumes.

The femtosecond laser-exposure process can be seen as moving an ellipsoid-shaped interaction zone (resulting from a non-linear laser-matter interaction) across the glass structure to be carved; in our set-up, motion is driven by linear-motor moving stages. The shape and size of the laser-affected zone within the glass depends critically on the focusing conditions, i.e. the numerical aperture of the focusing objective as well as the laser wavelength and the pulse energy. With our apparatus, at the finest level of focusing, we can produce an ellipsoid of diameter  $\sim 2 \mu\text{m}$  on its short axes and length  $8 \mu\text{m}$  on the long one. The velocity of the motorized stages is coupled to the laser pulse repetition rate to optimize the etching rate, as this depends strongly on the deposited energy (or dose, typically expressed in  $\text{J mm}^{-2}$ ) [39].

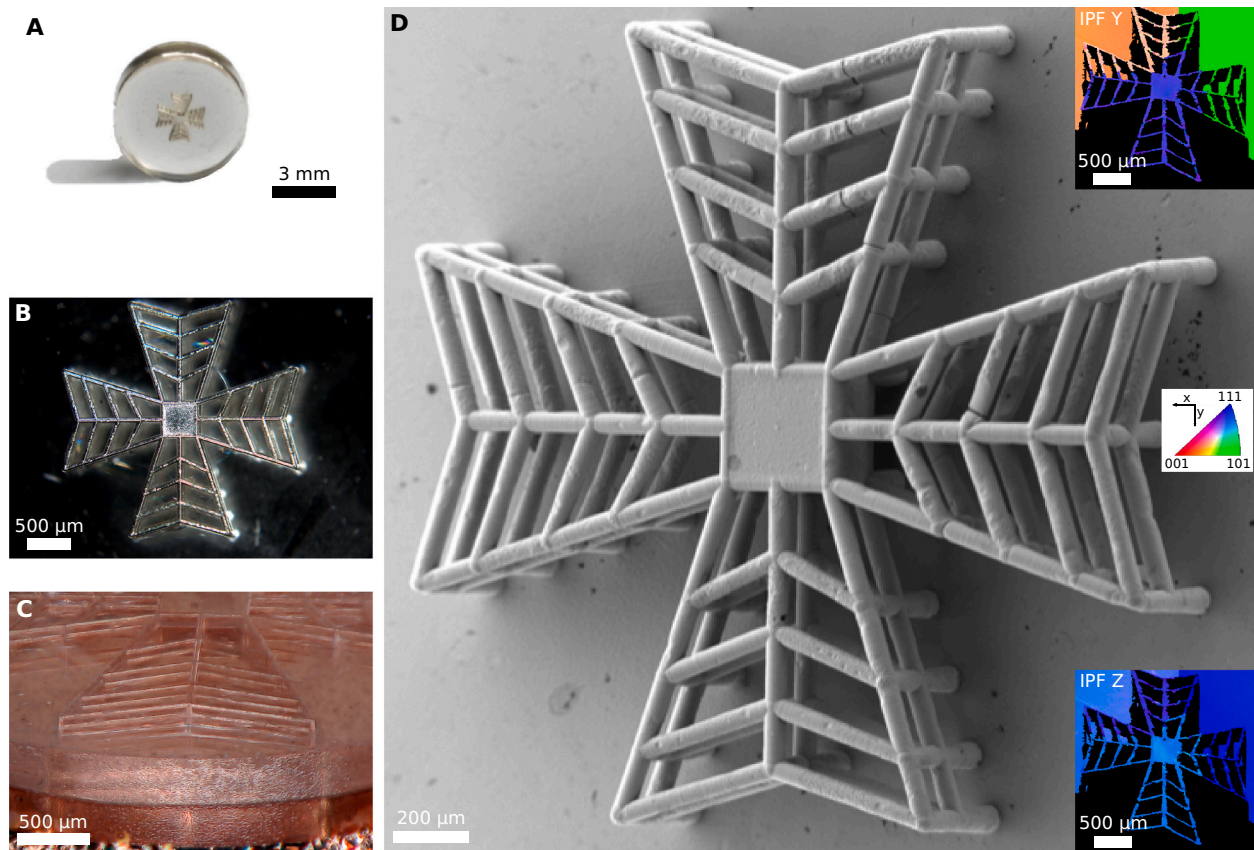


**Fig. 5.** Complex (Maltese cross) 3D structure produced in pure silver and pure copper. (A) and (B) Optical images of a silver cross embedded within its fused quartz mold. (C) Macroscopic image of a larger version of the same design produced in copper, also still contained within its fused quartz mold. (D) SEM image of the silver cross in (A) and (B) after mold removal. The related IPF images show the presence of 3 distinct grains, whose boundaries are made visible in the SEM image by the typical groove they have created along the casting surface.

Exposure parameters are set by several considerations. On one hand, thermal diffusion beyond the LAZ should be avoided; this limits the repetition rate to a maximum of about 1 MHz, which is the onset for thermal accumulation in fused silica [46]. An optimal deposited energy value of  $\sim 10 \text{ J mm}^{-2}$  (for HF 2.5% vol. etching) is reported to achieve the highest etching contrast between laser affected zones and pristine material. Considering a repetition rate of 900 kHz, the maximum optimal writing speed is  $\sim 15 \text{ mm s}^{-1}$  [39]. This is a very high value, such that operationally it is inertia, and in turn the achievable acceleration of the motorized stages used here (maximum acceleration of  $\sim 50 \text{ mm s}^{-2}$ ) that will limit the maximum attainable speed for  $\mu\text{m}$ -scale patterns to values well below the above limit. This adds a dependence of the maximum average glass pattern printing velocity on the intricacy of the pattern. For example, to pattern the structures in Figs. 2 and 5, the average speeds of our stages were  $\sim 1.0$  and  $\sim 1.45 \text{ mm s}^{-1}$ , respectively; however, these values are defined by technical limitations of our setup. Other commercial motorized stages can reach accelerations of around  $10 \text{ m s}^{-2}$ . This would result in average writing speeds of  $\sim 14.1$  and  $\sim 20.1 \text{ mm s}^{-1}$  for the previous examples; therefore, one can in practice reach the theoretical speed limit outlined above.

Additional features of the process are also to be noted, on both fronts of limitations and potential. Pressure infiltration is, as expected, capable of intimately replicating nanometric features. The minimum channel size that can be infiltrated is ruled by the pressure required to overcome the molten metal surface tension that opposes its flow into tiny mold cavities. This is given by the Young-Laplace equation [30], according to which the capillary pressure differential roughly equals the metal surface tension divided by the channel width. Surface tensions of most metals are on the order of  $1 \text{ J m}^{-2}$ ; hence, a pressure of 10 MPa, which is

technically achievable, should drive metal into features as fine as 100 nm. This is in keeping with the observed fidelity with which the infiltrated metal reproduces the carved glass structure in samples of this work.

The present process is therefore limited in terms of resolution by the controllable size of the LAZ which, due to the non-linear nature of the process by which it is formed, can itself be significantly smaller than the optical waist in the focused path of the laser beam (in our case  $\approx 1.8 \mu\text{m}$  at a laser wavelength of 1030 nm) as illustrated elsewhere [47]. In its versions presented here the process has a resolution of  $2 \mu\text{m}$ ; however, for these reasons, this may be reduced in future work. For example, an additional approach to reduce the laser beam waist further, and in turn, the size of the laser affected zone, is to use shorter wavelengths, for instance by frequency doubling or tripling common Ytterbium-based laser sources, reaching out to the UV exposure regime.

A limitation of the present process is that it is a priori not amenable to process alloys that contain elements, the oxide of which is more stable than silica (for example aluminum, titanium or magnesium) or to process metals with melting temperature higher than the mold annealing temperature,  $\sim 1200 \text{ }^\circ\text{C}$  for fused quartz. It also tends to produce large-grained structures, which has advantages (e.g., high conductivity) and disadvantages (e.g., absence of grain boundary hardening or the formation of visible grain boundary grooves along the metal surface; see Fig. 5D). Finally, the process is well suited for the production of multi-scale structures (as in Fig. 4) and it offers, when making multiscale structures, scope for efficiency gains in production if laser parameters are dynamically adjusted during printing. One could indeed dynamically alter lens parameters (for example by using a spatial light modulator) and beam energy, so as to vary both the laser spot shape and size

while maintaining optimal exposure conditions. This possibility might largely increase the volumetric speed and so provide opportunities for the rapid production of multiscale structures. For example, just by tuning the beam energy, the ellipsoidal LAZ can vary from  $\sim 1$  to  $\sim 2.5$   $\mu\text{m}$  and from  $\sim 8$  to  $\sim 20$   $\mu\text{m}$  in short and long axis dimensions, respectively; this corresponds to an order of magnitude (dynamic) change in voxel volume [47].

Building on the extensive survey of metal freeform microfabrication that is given in Ref [19], the production speed of the microcasting process presented here is compared in Fig. 6 with alternative 3D metal freeform manufacturing techniques. Specifically, in Fig. 6A, the fabrication speed is normalized by the voxel size, which is in essentially all such processes assumed to be a cylinder with a diameter equal to the dimension read in the horizontal axis. Assuming a roughly equiaxed cylinder, one can obtain estimations of the volumetric production rate (for a more detailed description we refer to [19]). As seen, comparing feature sizes and production rates of the present process with current alternatives places it in the top right corner, showing that it stands out in terms of achievable production speeds. Such higher fabrication rates enable the industrialization of the process and the large-scale production of 3D components. In parallel, Fig. 6B displays a measure of the metal microstructural soundness, namely the ratio of measured to theoretical elastic modulus, using in this graph data and graph formats from Ref. [20], together with data for our samples reported in the Supplementary material, Tables S1 and S2. The pronounced porosity, and thus large spread in elastic properties, exhibited by most of the structures obtained by current micron-scale additive micromanufacturing processes other than local electroplating underline another major advantage of the microcasting process, namely the metallurgical soundness of the structures that it produces. For example, the electrical or thermal conductivity in metal structures produced by the present process will be as high as in the same pristine bulk metal, enabling micro-components and devices with optimal electrical or thermal performance. This is a feature that the present process only shares with electrodeposition, a process capable of finer resolution than the present process, albeit with far lower achievable production rates.

Moving forward, a few remaining challenges will have to be addressed for the present process to be improved or for it to enter commercial production. As seen, the pressure infiltrated metal

reproduces with precision even minute details, below 100 nm in size, along the inner mold surface, see Fig. 3; thus, improving the roughness of the molds is the next step in producing even smoother micro-cast products. A challenge, omnipresent in metal casting, is feeding solidification shrinkage of the metal. At the macro-scale there are well-known recipes to this end, directional solidification towards a riser being one of the main approaches. In the present instance, given the far smaller part dimensions, the influence exerted by capillary forces may still cause the formation and retention of tiny pores within the metal (perhaps cavities outlined in Fig. 3 are of this nature) or may lead to other defects, such as the grain boundary grooves apparent in Fig. 5. Finally, mastering the inner microstructural development of micron-scale cast metals and alloys is an area where much remains to be learned.

In conclusion, we have demonstrated that geometrically complex interconnected multiscale components up to a few millimeters in size and freely shaped to micrometric resolution can be made of fully dense metal via a novel, freeform manufacturing process that combines fs-laser glass micromachining with metal pressure infiltration. The process is suited for engineering metals that are inert in contact with silica, including silver, copper, gold and their alloys, and has the potential for higher large-scale production rates compared to existing technology. The resulting glass/metal combinations enable new device architectures for applications in a wide range of areas in microtechnology. Alternatively, by mold dissolution, this process fills a gap in microfabrication because it gives the ability to turn, as is done at the macro-scale, to casting when monolithic metallic parts of high geometrical complexity are to be produced.

#### 4. Methods

The glass molds were fabricated using fs laser micromachining followed by wet chemical etching according to a known process described in the literature [7]. We used an Ytterbium-fiber amplifier laser (Yuzu, manufactured by Amplitude, Bordeaux, France) emitting 270 fs pulses at a wavelength of 1030 nm at a repetition rate of 800 kHz, with an energy of 240 nJ (average power after the objective of about 190 mW). The laser is focused in the specimen using a 0.4-numerical aperture objective to a measured waist of 1.9  $\mu\text{m}$  at the focal point. The substrate used is a UV-grade fused quartz plate (Heraeus HOQ 310), 800  $\mu\text{m}$ -thick, and 25

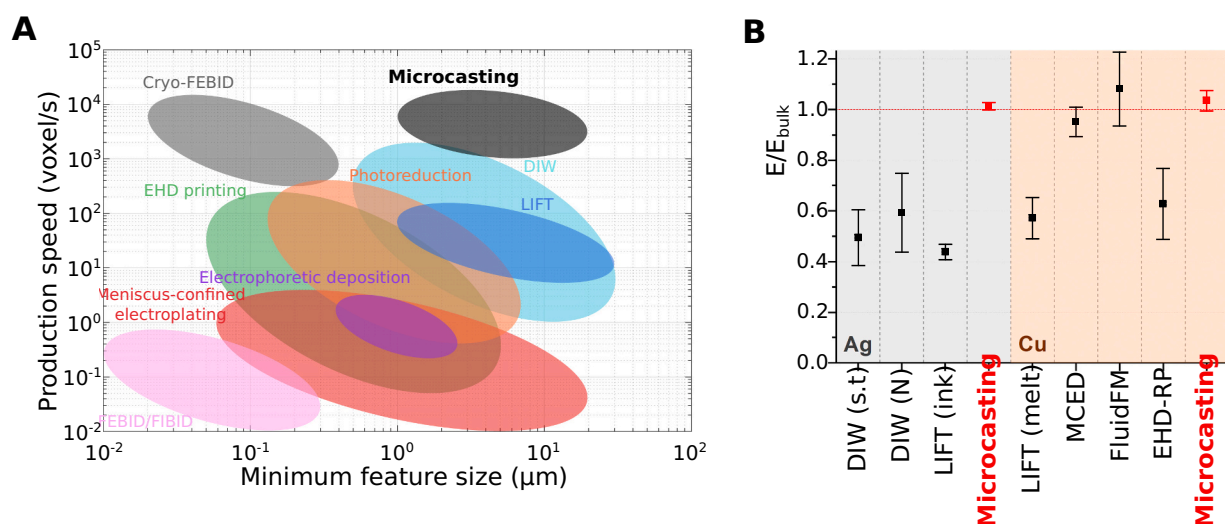


Fig. 6. (A) Qualitative comparison of achievable production speeds with alternative 3D freeform metal microfabrication processes (redrawn from [19]): Direct Ink Writing (DIW), Electrohydrodynamic Printing (EHD printing), Laser-Assisted Electrophoretic Deposition, Laser-Induced Forward Transfer (LIFT), Meniscus-Confined Electroplating, Laser-Induced Photoreduction, Focused Electron/Ion Beam Induced Deposition (FEBID/FIBID), Cryo-FEBID. (B) Comparison of measured elastic modulus normalized by theoretical elastic modulus obtained by different techniques on silver and copper structures: DIW (shear thinning), DIW (Newtonian), LIFT (ink), LIFT (melt), Meniscus-confined electrodeposition (MCED), Confined electro-deposition in liquid (FluidFM), Electrohydrodynamic Redox Printing (EHD-RP). Error bars represent measured standard deviation (redrawn from [20]).

mm-square. The substrate is moved with linear stages (Micos - UPS 150). Following laser exposure, the specimen is etched for several hours in a 2.5% HF acid bath at room temperature. In order to fit the dimensional requirements of the chamber used for metal infiltration, the substrates are cut into circular disks of 6 mm diameter to produce the molds into which the desired shapes to be injected are laser-patterned and subsequently etched.

The setup used for pressure infiltration consists of a refractory stainless steel (UNS S31400) chamber in which an alumina crucible prevents contact of the steel chamber with a graphite crucible that contains both the mold and the metal (see Fig. 1). Once mold and metal are placed within the graphite crucible, the infiltration chamber is bolted shut at its top. The top of the chamber contains a carbon foil to seal the closure and is connected to a vacuum pump and an argon bottle through a pipe, in which a K-type thermocouple is also introduced in order to monitor the temperature during infiltration by placing the thermocouple tip 1 mm above the melt. The chamber is evacuated (usually to  $\sim 0.06$  mbar) and positioned within an induction coil using an overhead crane. A GMF12 CELES (Lautenbach-France) induction furnace is utilized to heat up the ensemble, to 1000 °C in the case of silver and 1100 °C for infiltration with copper or gold. Once the target temperature is reached, the chamber is pressurized with an inert gas (Argon N48, typically at  $\sim 1.5$  MPa for structures of minimum feature size exceeding 1.5  $\mu\text{m}$ , or 5 MPa otherwise). Subsequently, the chamber is lowered until its bottom is in contact with a water-refrigerated copper chill, maintaining the pressure and also with the induction furnace turned on, in order to create a vertical temperature gradient to promote directional solidification. Once the solidification temperature is reached on the thermocouple reading, the chamber is cooled further and then kept at  $\sim 600$  °C during 1 h in order to relieve internal stresses caused by differential shrinkage between the mold and the metal. Heating is then stopped and the substrate-metal component is removed once it has reached room temperature. Pure silver (Figs. 2, 4A, 5A-B, D), gold (Fig. 3) or copper (Fig. 5C), all of 99.99 wt% purity, were utilized as infiltrant metals as well as a silver-copper alloy (79wt%Ag-21wt%Cu) (Fig. 4C-D). To produce cast metal structures released from their mold, in a final step the fused quartz mold was dissolved in high concentration HF during approximately 12 h (Figs. 2, 3, 5D).

#### 4.1. Materials characterization

Scanning electron microscopy images were obtained at 3 kV using a Zeiss® GeminiSEM 300 (Oberkochen, Germany) equipped with a standard Everhart-Thornley secondary-electron detector and an Oxford Instrument EDS detector. EBSD images were acquired at 25 kV using a Zeiss® SEM Gemini450 (Oberkochen, Germany) equipped with a symmetry CMOS, operating with Aztec acquisition and data treatment software (Oxford Instruments, UK). Optical micrographs were taken with a Hirox digital microscope KH-8700 (Tokyo, Japan).

Composition gradients near the interface of the host substrate/metal, exposed by conventional grinding and polishing of infiltrated beams still embedded in the fused quartz mold (Fig. S1B), were analyzed by Energy-dispersive X-ray spectroscopy (EDS) in the scanning electron microscope operated at 10 kV (Fig. S2). The X-ray intensity at the metal-silicon dioxide boundary was modeled with CASINO Monte Carlo software v2.5 (Sherbrooke, Canada) assuming a 10 kV electron beam, beam size 5 nm and 10,000 electrons. A TI 950 Triboindenter (Hysitron® Corporation, Minneapolis, MN) with a load cell of 10,000  $\mu\text{N}$  and a diamond Berkovich indenter tip was used to measure both the hardness and elastic modulus of the cast from cross-sections of trusses still embedded in the fused quartz substrate (similar to what is seen in Fig. 3E). Quasi-static indentations were made to a maximum load of 8000  $\mu\text{N}$  for silver and to 3000  $\mu\text{N}$  for copper, the loads being selected in correlation with the trusses' cross-sections (150  $\times$  150  $\mu\text{m}$  for Ag silver and 25  $\times$  25  $\mu\text{m}$  for copper) to minimize the elastic influence of the substrate and to be able to indent 4 times on each specimen. The loading-holding-unloading

sequence was of 5–2–5 s and the data were analyzed according to the Oliver-Pharr procedure [48].

#### Declaration of competing interest

Four of the present authors (CD, RC, YB and AM) are inventors on awarded European and US patents, application numbers of which are: US 2018304352 - WO 2017081635, applied for by École Polytechnique Fédérale de Lausanne (EPFL). SP, whose contribution to the work reported here was performed entirely while an employee of EPFL, is now pursuing commercialization of this technology for the production of microscopic decorative objects with a startup company named JARYS sàrl (this is, at this date, the only commercial application of the present microcasting process). LB, EC, LD, YT and FE declare no competing interest.

#### Acknowledgments

The authors thank Dr. C. Cayron, at Laboratory of Thermomechanical Metallurgy-EPFL, for his help in the EBSD data acquisition. The Galatea laboratory acknowledges with gratitude the sponsoring of the chair by Richemont International SA. The Laboratory of Mechanical Metallurgy acknowledges funding of this work by internal laboratory funds provided by EPFL.

#### CRediT authorship contribution statement

AM and YB designed the research and formulated the general concept exposed here. CD, RC, YB and AM conceived and produced first demonstrations of the process described here. Experiments and results presented here were produced mainly by LB and EC, while SP, LD, FE and TY contributed relevant experiments upstream of those reported here. The article text was mainly written by LB, EC, YB and AM, while figures were produced by LB and EC.

#### Data and materials availability

All data is available in the main text or the Supporting information.

#### Appendix A. Supplementary data

Supplementary data to this article can be found online at <https://doi.org/10.1016/j.jmapro.2021.06.002>.

#### References

- [1] Fundamentals of microfabrication: The science of miniaturization, Second edition. CRC Press; 2018. doi:<https://doi.org/10.1201/9781482274004>.
- [2] Maruo S, Nakamura O, Kawata S. Three-dimensional microfabrication with two-photon-absorbed photopolymerization. *Opt Lett* 1997;22:132–4. <https://doi.org/10.1364/OL.22.000132>.
- [3] Maruo S, Ikuta K. Three-dimensional microfabrication by use of single-photon-absorbed polymerization. *Appl Phys Lett* 2000;76:2656–8. <https://doi.org/10.1063/1.126742>.
- [4] Kawata S, Sun H-B, Tanaka T, Takada K. Finer features for functional microdevices. *Nature* 2001;412:697–8. <https://doi.org/10.1038/35089130>.
- [5] Kondo Y, Qiu J, Mitsuyu T, Hirao K, Yoko T. Three-dimensional microdrilling of glass by multiphoton process and chemical etching. *Jpn J Appl Phys* 1999;38:L1146–8. <https://doi.org/10.1143/JJAP.38.L1146>.
- [6] Marcinkevičius A, Juodkaziš S, Watanabe M, Miwa M, Matsuo S, Misawa H, et al. Femtosecond laser-assisted three-dimensional microfabrication in silica. *Opt Lett* 2001;26:277. <https://doi.org/10.1364/OL.26.000277>.
- [7] Bellouard Y, Said A, Dugan M, Bado P. Fabrication of high-aspect ratio, microfluidic channels and tunnels using femtosecond laser pulses and chemical etching. *Opt Express* 2004;12:2120. <https://doi.org/10.1364/OPEX.12.002120>.
- [8] Chin SY, Dikshit V, Meera Priyadarshini B, Zhang Y. Powder-based 3D printing for the fabrication of device with micro and mesoscale features. *Micromachines* 2020; 11:658. <https://doi.org/10.3390/mi11070658>.
- [9] Becker EW, Ehrfeld W, Hagmann P, Maner A, Münchmeyer D. Fabrication of microstructures with high aspect ratios and great structural heights by synchrotron radiation lithography, galvanofarming, and plastic moulding (LIGA process).

- Microelectron Eng 1986;4:35–56. [https://doi.org/10.1016/0167-9317\(86\)90004-3](https://doi.org/10.1016/0167-9317(86)90004-3).
- [10] Lorenz H, Despont M, Vettiger P, Renaud P. Fabrication of photoplastic high-aspect ratio microparts and micromolds using SU-8 UV resist. *Microsyst Technol* 1998;4: 143–6. <https://doi.org/10.1007/s005420050118>.
- [11] Melngailis J. Focused ion beam technology and applications. *J Vac Sci Technol B* 1987;5:469. <https://doi.org/10.1116/1.583937>.
- [12] Reyntjens S, Puers R. A review of focused ion beam applications in microsystem technology. *J Micromech Microeng* 2001;11:287–300. <https://doi.org/10.1088/0960-1317/11/4/301>.
- [13] Volkert CA, Minor AM. Focused ion beam microscopy and micromachining. *MRS Bull* 2007;32:389–99. <https://doi.org/10.1557/mrs2007.62>.
- [14] Xu J, Wang X, Wang C, Yuan L, Chen W, Bao J, et al. A review on micro/nanofabrication to fabricate 3D metallic structures. *Adv Mater n.d.;n/a:2000893*. doi: <https://doi.org/10.1002/adma.202000893>.
- [15] Hanada Y, Sugioka K, Midorikawa K. Selective metallization of photostructurable glass by femtosecond laser direct writing for biochip application. *Appl Phys A* 2008;90:603–7. <https://doi.org/10.1007/s00339-007-4373-2>.
- [16] Xu J, Wu D, Hanada Y, Chen C, Wu S, Cheng Y, et al. Electrofluidics fabricated by space-selective metallization in glass microfluidic structures using femtosecond laser direct writing. *Lab Chip* 2013;13:4608–16. <https://doi.org/10.1039/C3LC50962A>.
- [17] Xu J, Wu D, Ip J, Sugioka K. Vertical sidewall electrodes monolithically integrated into 3D glass microfluidic chips using water-assisted femtosecond-laser fabrication for in situ control of electrocatalysis. *RSC Adv* 2015;5:24072–80. <https://doi.org/10.1039/C5RA00256G>.
- [18] Tanaka T, Ishikawa A, Kawata S. Two-photon-induced reduction of metal ions for fabricating three-dimensional electrically conductive metallic microstructure. *Appl Phys Lett* 2006;88:081107. <https://doi.org/10.1063/1.2177636>.
- [19] Hirt L, Reiser A, Spolenak R, Zambelli T. Additive manufacturing of metal structures at the micrometer scale. *Adv Mater* 2017;29:1604211. <https://doi.org/10.1002/adma.201604211>.
- [20] Reiser A, Koch L, Dunn KA, Matsuura T, Iwata F, Fogel O, et al. Metals by micro-scale additive manufacturing: comparison of microstructure and mechanical properties. *Adv Funct Mater* 2020;30:1910491. <https://doi.org/10.1002/adfm.201910491>.
- [21] Wu P-W, Cheng W, Martini IB, Dunn B, Schwartz BJ, Yablonovitch E. Two-photon photographic production of three-dimensional metallic structures within a dielectric matrix. *Adv Mater* 2000;12:1438–41 [doi:10.1002/1521-4095(200010)12:19<1438::AID-ADMA1438>3.0.CO;2-Y].
- [22] Saleh MS, Hu C, Panat R. Three-dimensional microarchitected materials and devices using nanoparticle assembly by pointwise spatial printing. *Sci Adv* 2017;3: e1601986. <https://doi.org/10.1126/sciadv.1601986>.
- [23] Wilkinson NJ, Smith MAA, Kay RW, Harris RA. A review of aerosol jet printing—a non-traditional hybrid process for micro-manufacturing. *Int J Adv Manuf Technol* 2019;105:4599–619. <https://doi.org/10.1007/s00170-019-03438-2>.
- [24] Oran D, Rodrigues SG, Gao R, Asano S, Skylar-Scott MA, Chen F, et al. 3D nanofabrication by volumetric deposition and controlled shrinkage of patterned scaffolds. *Science* 2018;362:1281–5. <https://doi.org/10.1126/science.aau5119>.
- [25] Utke I, Michler J, Winkler R, Plank H. Mechanical properties of 3D nanostructures obtained by focused electron/ion beam-induced deposition: a review. *Micromachines* 2020;11:397. <https://doi.org/10.3390/mi11040397>.
- [26] Vyatskikh A, Delalande S, Kudo A, Zhang X, Portela CM, Greer JR. Additive manufacturing of 3D nano-architected metals. *Nat Commun* 2018;9:593. <https://doi.org/10.1038/s41467-018-03071-9>.
- [27] Ercolano G, Zambelli T, van Nesselroy C, Motenko D, Vörös J, Merle T, et al. Multiscale additive manufacturing of metal microstructures. *Adv Eng Mater* 2020; 22:1900961. <https://doi.org/10.1002/adem.201900961>.
- [28] Reiser A, Lindén M, Rohner P, Marchand A, Galinski H, Sologubenko AS, et al. Multi-metal electrohydrodynamic redox 3D printing at the submicron scale. *Nat Commun* 2019;10:1853. <https://doi.org/10.1038/s41467-019-09827-1>.
- [29] Braun TM, Schwartz DT. The emerging role of electrodeposition in additive manufacturing. *Interface Mag* 2016;25:69–73. <https://doi.org/10.1149/2.F071611f>.
- [30] N. Eustathopoulos, M.G. Nicholas, B. Drevet. Wettability at high temperatures. vol. 3. Pergamon Press, Inc.; 1999.
- [31] Baumeister G, Mueller K, Ruprecht R, Hausselt J. Production of metallic high aspect ratio microstructures by microcasting. *Microsyst Technol* 2002;8:105–8. <https://doi.org/10.1007/s00542-001-0132-z>.
- [32] Baumeister G, Hausselt J, Ruprecht R. Microcasting of parts made of metal alloys. *Microsyst Technol* 2004;10:261–4. <https://doi.org/10.1007/s00542-003-0363-2>.
- [33] Krebs J, Rao SI, Verheyden S, Miko C, Goodall R, Curtin WA, et al. Cast aluminium single crystals cross the threshold from bulk to size-dependent stochastic plasticity. *Nat Mater* 2017;16:730–6. <https://doi.org/10.1038/nmat4911>.
- [34] Sun Z, Vladimirov G, Nikolaev E, Velasquez-Garcia LF. Exploration of metal 3-D printing technologies for the microfabrication of freeform, finely featured, mesoscaled structures. *J Microelectromech Syst* 2018;27:1171–85. <https://doi.org/10.1109/JMEMS.2018.2875158>.
- [35] Siegel AC, Bruzewicz DA, Weibel DB, Whitesides GM. Microsolidics: fabrication of three-dimensional metallic microstructures in poly(dimethylsiloxane). *Adv Mater* 2007;19:727–33. <https://doi.org/10.1002/adma.200601787>.
- [36] Du D, Liu X, Korn G, Squier J, Mourou G. Laser-induced breakdown by impact ionization in SiO<sub>2</sub> with pulse widths from 7 ns to 150 fs. *Appl Phys Lett* 1994;64: 3071–3. <https://doi.org/10.1063/1.111350>.
- [37] Glezer EN, Milosavljevic M, Huang L, Finlay RJ, Her T-H, Callan JP, et al. Three-dimensional optical storage inside transparent materials. *Opt Lett* 1996;21:2023. <https://doi.org/10.1364/OL.21.002023>.
- [38] Kiyama S, Matsuo S, Hashimoto S, Moriguchi Y. Examination of etching agent and etching mechanism on femtosecond laser microfabrication of channels inside vitreous silica substrates. *J Phys Chem C* 2009;113:11560–6. <https://doi.org/10.1021/jp900915r>.
- [39] Rajesh S, Bellouard Y. Towards fast femtosecond laser micromachining of fused silica: the effect of deposited energy. *Opt Express* 2010;18:21490. <https://doi.org/10.1364/OE.18.021490>.
- [40] Hasse K, Huber G, Kränkel C. Selective etching of fs-laser inscribed high aspect ratio microstructures in YAG. *Opt Mater Express* 2019;9:3627. <https://doi.org/10.1364/OME.9.003627>.
- [41] Madani-Grasset F, Bellouard Y. Femtosecond laser micromachining of fused silica molds. *Opt Express* 2010;18:21826. <https://doi.org/10.1364/OE.18.021826>.
- [42] Schaap A, Bellouard Y. Molding topologically-complex 3D polymer microstructures from femtosecond laser machined glass. *Opt Mater Express* 2013;3:1428. <https://doi.org/10.1364/OME.3.001428>.
- [43] Wu B, Heidelberg A, Boland JJ, Sader JE, Sun Li. Microstructure-hardened silver nanowires. *Nano Lett* 2006;6:468–72. <https://doi.org/10.1021/nl052427f>.
- [44] Pharr GM, Oliver WC. Nanoindentation of silver-relations between hardness and dislocation structure. *J Mater Res* 1989;4:94–101. <https://doi.org/10.1557/JMR.1989.0094>.
- [45] Ma Q, Clarke DR. Size dependent hardness of silver single crystals. *J Mater Res* 1995;10:853–63. <https://doi.org/10.1557/JMR.1995.0853>.
- [46] Bellouard Y, Hongler M-O. Femtosecond-laser generation of self-organized bubble patterns in fused silica. *Opt Express* 2011;19:6807. <https://doi.org/10.1364/OE.19.006807>.
- [47] Bellouard Y, Barthel E, Said AA, Dugan M, Bado P. Scanning thermal microscopy and Raman analysis of bulk fused silica exposed to low-energy femtosecond laser pulses. *Opt Express* 2008;16:19520–34. <https://doi.org/10.1364/OE.16.019520>.
- [48] Oliver WC, Pharr GM. An improved technique for determining hardness and elastic modulus using load and displacement sensing indentation experiments. *J Mater Res* 1992;7:1564–83. <https://doi.org/10.1557/JMR.1992.1564>.